Journal of Materials Chemistry C

ROYAL SOCIETY OF CHEMISTRY

PAPER

View Article Online
View Journal

Cite this: DOI: 10.1039/d6tc00235h

First-principles high-throughput screening of ruthenium compounds for advanced interconnects

Gyungho Maeng, [a] Subeen Lim, [a] Bonggeun Shong [b] and Yeonghun Lee *[ac]

Received 22nd January 2026,
Accepted 13th March 2026

DOI: 10.1039/d6tc00235h

rsc.li/materials-c

As interconnect dimensions continue to shrink, the industry-standard copper faces a critical increase in resistivity, presenting a significant hurdle to overall device performance. To overcome this limitation, this work investigates the potential of ruthenium (Ru)-based compounds, encompassing binary, ternary, and quaternary systems, as viable alternatives to copper (Cu). Ruthenium is regarded as a strong candidate, owing to its inherent advantages in terms of reliability and more favorable resistivity scaling at reduced dimensions. Moreover, forming compounds offers an effective strategy to engineer novel properties, expanding the materials design space beyond the constraints of pure metals. Utilizing a high-throughput screening methodology, we systematically investigated a broad spectrum of 2106 Ru-based compounds to identify candidates with superior electronic transport and reliability characteristics. Consequently, we successfully identified a total of 61 promising candidates that exhibit excellent resistivity scaling behavior and enhanced reliability. These findings demonstrate that Ru-based compounds offer a viable pathway to overcome the scaling limitations of next-generation interconnects.

1 Introduction

Following the transition from aluminum, copper (Cu) has served as the long-standing industry-standard material for interconnects. However, as device dimensions scale down to the sub-nanometer regime, the industry faces a critical challenge: a dramatic increase in electrical resistivity, leading to significant resistance–capacitance (RC) delays that bottleneck overall device performance. This resistivity size effect is primarily driven by increased electron scattering at surfaces and grain boundaries phenomena, which become dominant when the feature size falls below the material's electron mean free path (MFP).[1–4] Fundamentally, this limitation stems from the relatively long MFP of Cu, approximately 39 nm,[5] which renders it highly sensitive to dimensional scaling.

In this context, ruthenium (Ru) has emerged as a compelling alternative candidate.[6–9] With a significantly shorter MFP of approximately 6.7 nm, Ru exhibits much lower sensitivity to scaling effects compared to Cu.[6,10] Furthermore, the practical implementation of Cu requires a thick, non-scalable diffusion barrier and liner layers, which consume a growing fraction of the interconnect volume and diminish the conductive cross-section.[11,12] Ru directly addresses this challenge, offering high cohesive energy that provides inherent reliability against electromigration,[5,13] and its chemical stability enables a simplified, barrierless integration scheme.[14,15] The viability of Ru has been well-established, having been previously investigated as a liner material for Cu, where it demonstrated excellent adhesion and gap-filling capabilities.[16–19] Notably, recent studies have confirmed the successful integration of Ru into fabrication processes as a primary conductor.[20–22]

While elemental Ru offers a clear path forward, even certain properties (*e.g.* reported suboptimal adhesion to some dielectrics[15,23]) might hinder its further optimization or tuning for the most scaled and integrated device architecture. The vast design space of binary, ternary, and quaternary compounds thus presents an even greater opportunity to engineer materials with superior properties. By combining elements, it becomes possible to tailor properties beyond what elemental Ru alone can offer, allowing for specific enhancements in electronic transport characteristics, improved interfacial compatibility with diverse dielectric layers, or even stronger interatomic bonding for superior reliability against electromigration.

To identify candidates that not only outperform elemental Cu but also possess robust integration potential, this work

[a] Department of Electronics Engineering, Incheon National University, Yeonsu-gu, Incheon 22012, Republic of Korea. E-mail: y.lee@inu.ac.kr
[b] Major in Advanced Materials and Semiconductor Engineering, Hanyang University, Ansan-si, Gyeonggi-do 15588, South Korea
[c] Research Institute for Engineering and Technology, Incheon National University, Yeonsu-gu, Incheon 22012, Republic of Korea

extends the conventional high-throughput screening of binary systems to comprehensively explore the expanded materials space of ternary and quaternary Ru-based compounds. We employ two key figures of merit: (1) the product of bulk resistivity and mean free path ($\rho_0 \times \lambda$), an intrinsic descriptor of scaling behavior where a lower value predicts more favorable conductivity at reduced dimensions;[5,24] (2) cohesive energy (E_{coh}), which serves as a proxy for reliability, signifying stronger inter-atomic bonding and thus enhanced resistance against electromigration and diffusion.[5,25] Especially, unlike previous studies that often present $\rho_0 \times \lambda$ values by individually categorizing each transport direction or focusing solely on the most conductive crystallographic orientation,[10,26,27] our work presents an averaged value that more realistically reflects the effective resistance in real interconnects, thereby considering the practical growth environment. This study thereby aims to identify novel compounds predicted to overcome current scaling limitations for future interconnects.

2 High-throughput screening

The theoretical framework for this study relies on high-throughput first-principles calculations based on density functional theory (DFT), executed with the Vienna *ab initio* Simulation Package (VASP).[28,29] For these calculations, the exchange–correlation functional was treated with the Perdew–Burke–Ernzerhof (PBE) formulation under the generalized gradient approximation (GGA),[30,31] and ion–electron interactions were described using pseudopotentials generated by the projector-augmented wave (PAW) method.[32,33] The effect of spin polarization was considered in all calculations.

To facilitate a broad and efficient materials search, we began by sourcing initial crystal structures from the Materials Project database *via* its Application Programming Interface (API).[34,35] These candidates were subsequently subjected to a multi-step screening process, depicted in Fig. 1, designed to identify the most promising materials. The screening criteria required that compounds be (1) metallic (band gap $E_G \leq 0$ eV), (2) thermodynamically stable (energy above the convex hull $E_{Hull} \leq 20$ meV per atom), and (3) structurally simple ($N_{atom} \leq 20$ atoms in the primitive unit cell).[36] Our choice of $E_{Hull} \leq 20$ meV per atom for thermodynamic stability is a deliberate and pragmatically motivated criterion. While strict thermodynamic stability ($E_{Hull} \leq 0$ eV per atom) is often theoretically preferred, it is known that not all stable compounds are synthesizable, nor are all unstable compounds impossible to synthesize.[37] Thus, we selected 20 meV per atom as a threshold slightly above the DFT-calculated known median of metastability of 15 ± 0.5 meV per atom.[36]

For the selected candidates, static self-consistent field calculations were set up using standardized input parameters generated *via* the Pymatgen library.[38] To simplify the calculation methodology, we leveraged the pre-relaxed structural data directly from the Materials Project database, where geometries are optimized with their convergence criteria (ionic step energy convergence $\leq 5 \times 10^{-4} \times N_{atoms}$ eV, where N_{atoms} refers to the number of atoms). Consequently, these optimized structures were used directly for electronic structure calculations without further relaxation. The plane-wave energy cutoff was set to 520 eV with a *k*-point density of 100 Å^{-3}. To properly account for magnetic effects, we directly retrieved and utilized the optimized magnetic ground states for each structure from the Materials Project database. Hubbard *U* corrections were applied to compounds containing oxygen, following the Materials Project compatibility standards.

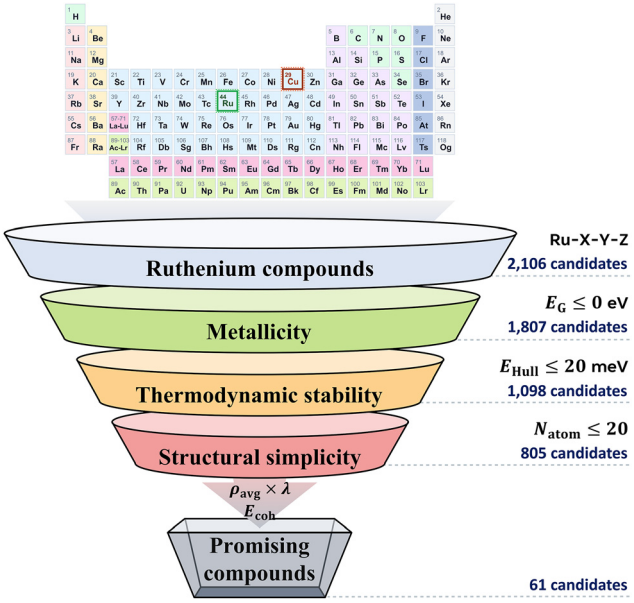

Fig. 1 High-throughput screening procedure for promising ruthenium compounds. Highlighted elements in the periodic table represent copper, the standard interconnect material, and ruthenium, the target element in this study.

Electronic transport properties were evaluated using the semiclassical Boltzmann transport theory implemented in the BoltzTraP2 code.[39,40] To ensure numerical accuracy in the transport integrals, non-self-consistent field calculations were performed on a significantly dense *k*-point mesh, utilizing at least 50 000 grid points per reciprocal atom. The electrical conductivity tensor $\sigma_{\alpha\beta}$ is defined as:

$$\sigma_{\alpha\beta} = \frac{e^2}{8\pi^3} \sum_n \int_{BZ} d^3k \tau_n(\mathbf{k}) v_{\alpha,n}(\mathbf{k}) v_{\beta,n}(\mathbf{k}) \frac{df_{FD}(E)}{dE}\bigg|_{E=E_n(\mathbf{k})} \quad (1)$$

where α and β are tensor indices, e is the elementary charge, and n denotes the band index. The integration is performed over the Brillouin zone (BZ), with $\tau_n(\mathbf{k})$ and $v_{\alpha,n}(\mathbf{k})$ representing the carrier relaxation time and the group velocity for each tensor direction, respectively, where $\mathbf{k}$ is the wavevector. The term $df_{FD}(E)/dE$ corresponds to the Fermi window function derived from the Fermi–Dirac distribution $f_{FD}(E)$, and $E_n(\mathbf{k})$ is the eigenenergy. We adopted the constant mean-free-path approximation, where the relaxation time is defined as $\tau_n(\mathbf{k}) = \lambda/|v_n(\mathbf{k})|$. It should be noted that this approximation may not perfectly capture the scattering anisotropies with complex Fermi surface topologies. Nevertheless, previous studies

demonstrate that such deviations do not lead to significant errors in the preliminary screening of interconnect candidates.[7,41] Under this assumption, eqn (1) can be reformulated to express conductivity per unit MFP:

$$\frac{\sigma_{\alpha\beta}}{\lambda} = \frac{1}{\rho_{\alpha\beta} \times \lambda} = \frac{e^2}{8\pi^3} \sum_n \int_{\mathrm{BZ}} \mathrm{d}^3k \frac{v_{\alpha,n}(\mathbf{k}) v_{\beta,n}(\mathbf{k})}{|\mathbf{v}_n(\mathbf{k})|} \frac{\mathrm{d}f_{\mathrm{FD}}(E)}{\mathrm{d}E}\Big|_{E=E_n(\mathbf{k})} \quad (2)$$

This derivation indicates that the calculated $\sigma_{\alpha\beta}/\lambda$ is the inverse of $\rho_{\alpha\beta} \times \lambda$. Therefore, we employ $\rho_{\alpha\beta} \times \lambda$ as the primary intrinsic figure of merit to assess the intrinsic scaling behavior of resistivity, which is particularly relevant for ultranarrow interconnect applications.

3 Simulation results and discussion

To evaluate the intrinsic transport properties of the screened compounds, a robust scalar descriptor is required to condense the tensorial outputs of electronic transport calculations. For compounds with cubic symmetry, the isotropic diagonal components allow for a direct scalar representation. However, for non-cubic structures, directional anisotropy necessitates a systematic averaging procedure to ensure a consistent comparison across diverse crystal symmetries. In this work, we primarily define an effective $\rho_{\mathrm{avg}} \times \lambda$ based on a conductivity-averaging scheme. Specifically, a diagonal-only arithmetic average of the three conductivity-proportional components (σ_{xx}/λ, σ_{yy}/λ, and σ_{zz}/λ) in eqn (2) is evaluated. This approach represents an effective-medium transport scenario in which multiple crystallographic conduction channels contribute concurrently to the overall electrical response, analogous to a parallel combination of transport pathways. Such a description is appropriate for bulk and polycrystalline materials, where electrical current responds collectively to an applied field rather than being confined to a single crystallographic direction. As a result, the conductivity-based average serves as an effective descriptor of the overall transport performance while minimizing the impact of unfavorable high-resistivity directions.[42] Accordingly, this conductivity-based averaging scheme is adopted throughout the main text to ensure a consistent comparison of materials with varying crystal symmetries in the context of high-throughput screening.

For comparison, an alternative resistivity-based averaging scheme $\left(\rho^*_{\mathrm{avg}} \times \lambda\right)$ is also considered. In this case, an arithmetic average of the resistivity-proportional components ($\rho_{xx} \times \lambda$, $\rho_{yy} \times \lambda$, and $\rho_{zz} \times \lambda$) is taken. This averaging method emphasizes the contribution of individual transport directions equally and is therefore more closely associated with transport scenarios in which directional resistances are effectively combined in series.[42] It can be assumed that under the confinement conditions, in narrow wire-like structures, the current is constrained to traverse less favorable crystallographic orientations without the possibility of bypassing high-resistivity pathways. Consequently, this definition highlights the influence of high-resistivity directions and provides an upper bound on the electrical resistivity that a material system may theoretically attain. While this resistivity-based average is valuable for assessing the theoretical limit of transport degradation and for examining directional sensitivity, the conductivity-based averaging scheme is employed as the primary descriptor in this work, as it is not only more commonly employed in first-principles transport studies for comparative materials screening[7,43,44] but also more directly comparable to experimentally measured thin-film resistivities. Plots based on the resistivity-based averaging scheme are therefore provided as complementary information in Section S1, SI (Fig. S1–S3), while the corresponding values for promising compounds are summarized in the last column of tables.

Based on the screening workflow described in Section 2, we first examined a total of 2106 Ru-based compounds, spanning binary, ternary, and quaternary systems. By applying a series of screening criteria, the initial materials space was narrowed to 805 metallic and thermodynamically viable phases. These compounds were subsequently evaluated using two key figures of merit: $\rho_{\mathrm{avg}} \times \lambda$ and the cohesive energy E_{coh}. To assess transport performance in a manner relevant to scaled interconnects, elemental Cu was considered as the primary benchmark material. The calculated values for Cu are $\rho_{\mathrm{avg}} \times \lambda = 6.70 \times 10^{-16}$ Ω m^2 and $E_{\mathrm{coh}} = 3.88$ eV. Recognizing that actual interconnect properties are governed not only by intrinsic transport metrics but also by harder-to-quantify factors such as process compatibility, thermal stability, and interfacial adhesion,[25,45] we note that materials slightly underperforming Cu in one metric may still offer superior overall integration potential. Furthermore, as our study aims to identify a broad and comprehensive list of promising compounds, considering these complex interdependencies, we allowed candidates with up to 20% higher $\rho_{\mathrm{avg}} \times \lambda$, and up to 20% lower E_{coh} compared to those of Cu for further consideration. Applying these criteria, a total of 61 promising Ru-based compounds are presented in Fig. 2. Among them, 23 candidates are binary phases, 38 are ternary phases, and no quaternary compounds satisfy the combined transport and stability requirements.

The comprehensive screening results for binary Ru-based compounds are summarized in Fig. 3. The shaded regions delineate performance benchmarks defined by elemental Cu, the current industry standard, and elemental Ru, which serves as a reference material in this study. As discussed above, the grey-shaded region represents an extended benchmark window introduced to avoid over-restrictive filtering based solely on intrinsic transport and cohesive energy metrics. This relaxed window is intended to preserve candidates that may exhibit advantageous secondary properties not explicitly captured by the present descriptors. Out of 93 binary compounds that satisfied our screening workflow, 23 compounds were identified within the defined performance window. Among these binary candidates, eight compounds—AlRu,[46,47] GaRu,[48] LuRu,[49] ScRu,[50,51] TaRu,[52,53] URu_3,[54,55] VRu,[56,57] and YbRu[58]—have been reported to be experimentally synthesizable, as verified through experimental reports within the Inorganic Crystal Structure Database (ICSD). Notably, AlRu has also

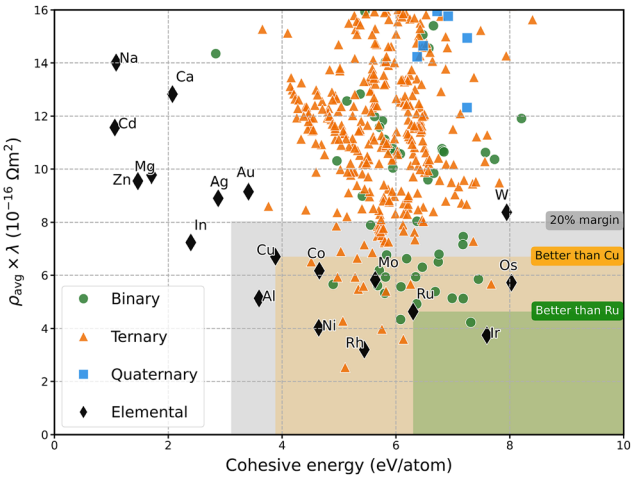

Fig. 2 The electrical properties as a function of cohesive energy for all screened Ru-based compounds. The elemental materials are marked with black diamonds. The shaded areas represent the parameter space where the performance is expected to be superior to that of each reference material, as well as the performance margin relative to the Cu material. Note that compounds with $\rho_{avg} \times \lambda$ over 16×10^{-16} Ω m^2 are omitted due to their predicted poor electrical performance.

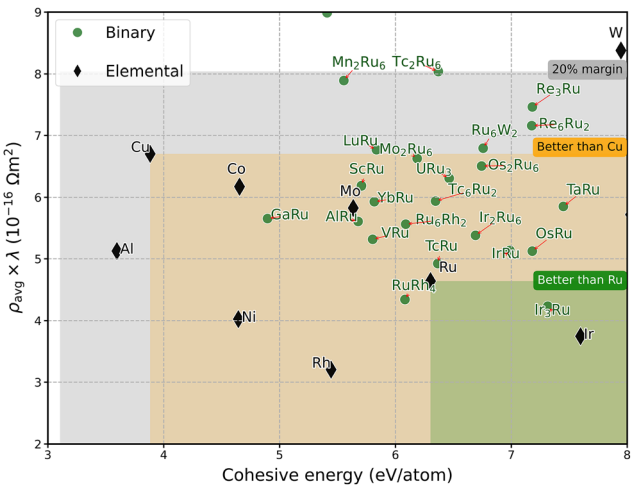

Fig. 3 Potential candidates among binary Ru compounds against Cu. The highlighted zones (orange and green) categorize compounds that exceed the performance of elemental Cu and Ru, respectively. A total of 23 binary candidates are identified within the 20% margin of Cu, representing the most promising system for advanced interconnect materials. Elemental benchmarks (Cu, Ru, *etc.*) are provided for comparative reference.

attracted recent attention as a potential alternative material for interconnect technology, having been experimentally evaluated as promising in prior research.[59] Detailed calculated properties and structural information for all selected binary compounds are provided in Table 1.

Fig. 4 presents the corresponding screening results for ternary Ru-based compounds. From an initial pool of 626 ternary phases, 38 compounds were identified within the defined performance window. Among the selected ternary candidates, six compounds—$CeGe_2Ru_2$,[60,61] CeP_2Ru_2,[62] $CeSi_2Ru_2$,[63,64] $EuGe_2Ru_2$,[65,66] $LaSi_2Ru_2$,[63] and USi_2Ru_2[67,68]—have been experimentally synthesized. Attempts to utilize these materials in interconnect applications have not yet been documented in the literature. The full list of ternary candidates and their calculated properties are summarized in Table 2. In contrast to the binary and ternary systems, none of the quaternary Ru-based compounds fall within our performance window. This absence is largely a consequence of the screening criteria applied during the initial screening stages rather than an inherent lack of electrical performance in complex compounds. As the number of constituent elements increases from binary to quaternary systems, the number of atoms constituting the primitive unit cell tends to increase to accommodate the required stoichiometry. Statistically, while only ~10% of binary compounds exceed the N_{atom} limit, this fraction increases to ~25% for ternary systems and drastically increases to ~51% for quaternary systems. Consequently, a significant portion of quaternary candidates were excluded prior to the transport evaluation due to this constraint.

Despite the identification of several promising Ru-based compounds within the defined performance window, safety and material feasibility considerations must be addressed for specific candidates. In particular, compounds containing beryllium (Be) require careful handling due to its well-established carcinogenicity, while technetium (Tc)- and uranium (U)-containing materials raise concerns associated with radioactivity. While these factors certainly pose significant challenges for conventional semiconductor manufacturing, their inclusion in this foundational screening is justified by the potential for unique material properties that may warrant their use in specialized applications and exhibit irreplaceable performance. Indeed, despite its carcinogenicity, Be is utilized in various field such as aviation, aerospace, and nuclear fusion due to its excellent properties. Similarly, radioactive materials containing Tc and U can also still be considered for use under strict safety measures when their superior properties justify their application in specialized fields. However, the use of such materials necessitates high-level engineering controls, comprehensive personal protective equipment, continuous environmental monitoring, and thorough training on safe handling procedures.[69–72] For the primary objective of this study, which is to provide a broad and exhaustive list of potentially useful materials for subsequent research, these data were included without arbitrary exclusion. Furthermore, while the number of compounds with confirmed experimental synthesizability may not be extensive, their selection based on a thermodynamic stability criterion ($E_{hull} \leq 20$ meV per atom) suggests a high potential for future experimental synthesis.

From a performance standpoint, our simulations indicate that, among the screened binary systems, only Ir_3Ru marginally outperforms elemental Ru, while all other candidates fall short of surpassing bulk Ru in the metrics considered here. A similar trend is observed for ternary systems, where none achieve performance exceeding that of elemental Ru. This observation is consistent with prior studies on Cobalt (Co)-based binary interconnect materials, which likewise reported few compounds (Co_3Ni, CoPt, and $CoPt_3$) outperforming elemental Co when evaluated using comparable intrinsic transport-related criteria.[73] This overall trend suggests that, when assessed solely

Table 1 Most promising Ru binary compounds

Chemical formula	Material ID	Crystal symmetry	Experimentally synthesized[a]		Total magnetization (μ_B)	Cohesive energy[b] (eV)	$\rho_{\alpha\beta} \times \lambda$ (10^{-16} Ω m^2)				
							$\rho_{xx} \times \lambda$	$\rho_{yy} \times \lambda$	$\rho_{zz} \times \lambda$	$\rho_{avg} \times \lambda$	$\rho^*_{avg} \times \lambda$
AlRu	mp-542569	Cubic	O	46 and 47	0	5.68	5.61	5.61	5.61	5.61	5.61
GaRu	mp-22320	Cubic	O	48	0	4.90	5.65	5.65	5.65	5.65	5.65
IrRu	mp-974421	Hexagonal			0	6.99	5.02	5.03	5.37	5.14	5.14
Ir_2Ru_6	mp-862620	Hexagonal			0	6.69	5.84	5.82	4.66	5.38	5.44
Ir_3Ru	mp-974358	Tetragonal			0	7.31	4.15	4.15	4.39	4.23	4.23
LuRu	mp-11495	Cubic	O	49	0	5.84	6.77	6.77	6.77	6.77	6.77
Mn_2Ru_6	mp-865045	Hexagonal			1.179	5.55	8.08	8.08	7.55	7.89	7.90
Mo_2Ru_6	mp-975834	Hexagonal			0	6.19	9.21	9.21	4.24	6.62	7.55
OsRu	mp-1220023	Hexagonal			0	7.18	5.62	5.62	4.35	5.12	5.20
Os_2Ru_6	mp-974326	Hexagonal			0	6.74	5.92	5.93	8.08	6.50	6.64
Re_3Ru	mp-974455	Orthorhombic			0	7.18	6.08	7.41	9.76	7.46	7.75
Re_6Ru_2	mp-974625	Hexagonal			0	7.18	8.52	8.53	5.42	7.16	7.49
$RuRh_4$	mp-1219522	Trigonal			0.001	6.08	6.31	3.75	3.75	4.34	4.61
Ru_6Rh_2	mp-1186926	Hexagonal			0	6.09	5.95	5.95	4.92	5.56	5.61
Ru_6W_2	mp-862655	Hexagonal			0	6.76	9.41	9.41	4.37	6.79	7.73
ScRu	mp-30867	Cubic	O	50 and 51	0	5.71	6.18	6.18	6.18	6.18	6.18
TaRu	mp-1601	Tetragonal	O	52 and 53	0	7.45	6.48	6.48	4.89	5.85	5.95
TcRu	mp-1217363	Hexagonal			0	6.37	5.25	5.25	4.37	4.92	4.96
Tc_2Ru_6	mp-867356	Hexagonal			0	6.37	8.51	8.51	7.24	8.04	8.09
Tc_6Ru_2	mp-861630	Hexagonal			0	6.35	7.08	7.09	4.49	5.94	6.22
URu_3	mp-1263	Cubic	O	54 and 55	0.003	6.46	6.30	6.30	6.30	6.30	6.30
VRu	mp-1395	Cubic	O	56 and 57	0.559	5.80	5.31	5.31	5.33	5.32	5.32
YbRu	mp-567116	Cubic	O	58	0	5.82	5.93	5.93	5.93	5.93	5.93

[a] The synthesizability of the materials was determined by referencing the compositions provided in the ICSD. [b] The cohesive energies are obtained from the materials project database.

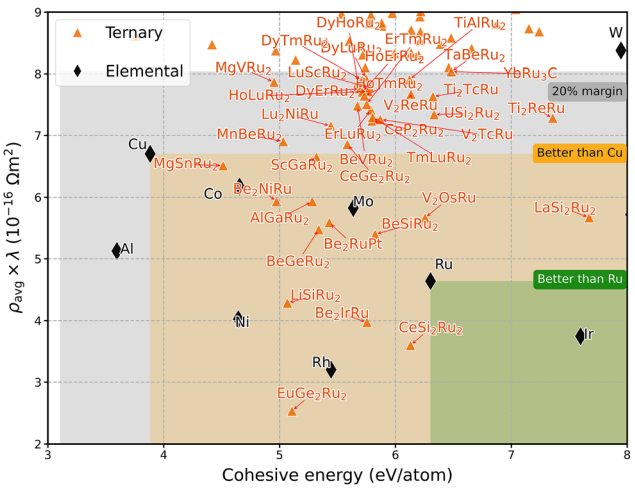

Fig. 4 High-throughput screening of ternary Ru compounds. The scatter plot maps the distribution of ternary candidates across the performance–stability design space. The shaded regions indicate the performance thresholds relative to each elemental property.

through intrinsic electronic transport indicators, it is intrinsically challenging for compound materials to simultaneously exceed the performance of their best elemental counterparts. The observed slight advantage of Ir_3Ru over elemental Ru, for instance, is highly influenced by the inherently superior electronic transport properties of its constituent Ir. Indeed, a broader analysis encompassing all metallic elemental materials alongside our binary compounds (Fig. S4) reveals that compound transport properties are often positioned between those of their constituent elements. While some compounds like Ru_6Rh_2, Tc_6Ru_2, Re_3Ru, and AlRu exhibit a higher resistivity factor than either constituent element, others, such as Ru_6W_2, $RuRh_4$, and TcRu, demonstrate properties falling between the electrical characteristics of their respective elemental components. This spectrum of performance analytically demonstrates that while complex atomic and electronic interactions are at play, compound formation predominantly redistributes, rather than inherently transcends, the intrinsic transport properties relative to their elemental building blocks.

To elucidate the fundamental physical origins of this systematic performance trend, we focused on binary compounds as an ideal model system. This targeted approach allows us to precisely isolate the intrinsic structure–property relationships governing A–B interactions, avoiding the confounding effects of multi-element structural complexity inherent in ternary and quaternary systems. Using the XenonPy toolkit,[74] we extracted 116 compositional descriptors, focusing on both the weighted average and weighted variance features to comprehensively capture the effective system properties and the degree of elemental dissimilarity within each compound. As shown in the Pearson correlation heatmaps (Fig. 5a), the average-related descriptors reveal that the effective van der Waals radius based on the universal force field (vdw_radius_uff) exhibits a positive correlation with $\rho_{avg} \times \lambda$ ($r = 0.44$) (detailed descriptions of the other variance descriptors are provided in Table S1, SI). This indicates that as the overall cell size of the compound increases, the intrinsic transport performance progressively degrades. Furthermore, these data reveal strong positive correlations ($r \geq 0.75$) between E_{coh} and thermodynamic stability metrics such as melting_point, evaporation_heat, and heat_of_formation. Since the melting point is widely used as a

Table 2 Most promising Ru ternary compounds

Chemical formula	Material ID	Crystal symmetry	Experimentally synthesized[a]		Total magnetization (μ_B)	Cohesive energy[b] (eV)	$\rho_{\alpha\beta} \times \lambda$ (10^{-16} Ω m^2)				
							$\rho_{xx} \times \lambda$	$\rho_{yy} \times \lambda$	$\rho_{zz} \times \lambda$	$\rho_{avg} \times \lambda$	$\rho^*_{avg} \times \lambda$
$AlGaRu_2$	mp-1183218	Cubic			0	5.28	5.93	5.93	5.93	5.93	5.93
$BeGeRu_2$	mp-862713	Cubic			0	5.34	5.48	5.48	5.48	5.48	5.48
$BeSiRu_2$	mp-867835	Cubic			0	5.83	5.40	5.40	5.40	5.40	5.40
$BeVRu_2$	mp-867874	Cubic			0	5.67	7.48	7.48	7.48	7.48	7.48
Be_2IrRu	mp-1183419	Cubic			0	5.75	3.97	3.97	3.97	3.97	3.97
Be_2NiRu	mp-1183421	Cubic			0	4.97	5.93	5.93	5.93	5.93	5.93
Be_2RuPt	mp-865021	Cubic			0	5.43	5.59	5.59	5.59	5.59	5.59
$CeGe_2Ru_2$	mp-22343	Tetragonal	O	60 and 61	0.594	5.58	9.36	8.77	4.61	6.85	7.58
CeP_2Ru_2	mp-574244	Tetragonal	O	62	0.428	5.80	9.32	8.96	5.11	7.23	7.80
$CeSi_2Ru_2$	mp-3566	Tetragonal	O	63 and 64	0.242	6.13	4.83	4.54	2.46	3.60	3.94
$DyErRu_2$	mp-1183783	Cubic			0	5.69	7.76	7.76	7.76	7.76	7.76
$DyHoRu_2$	mp-1183786	Cubic			0	5.68	7.86	7.86	7.86	7.86	7.86
$DyLuRu_2$	mp-1183818	Cubic			0	5.75	7.92	7.92	7.92	7.92	7.92
$DyTmRu_2$	mp-1184074	Cubic			0	5.71	7.90	7.90	7.90	7.90	7.90
$ErLuRu_2$	mp-1184363	Cubic			0	5.79	7.42	7.42	7.42	7.42	7.42
$ErTmRu_2$	mp-1184242	Cubic			0	5.75	7.51	7.51	7.51	7.51	7.51
$EuGe_2Ru_2$	mp-21417	Tetragonal	O	65 and 66	6.389	5.11	3.64	3.37	1.63	2.53	2.88
$HoErRu_2$	mp-976311	Cubic			0	5.71	7.71	7.70	7.72	7.71	7.71
$HoLuRu_2$	mp-973114	Cubic			0	5.77	7.71	7.71	7.72	7.71	7.71
$HoTmRu_2$	mp-1184831	Cubic			0	5.73	7.64	7.64	7.64	7.64	7.64
$LaSi_2Ru_2$	mp-5105	Tetragonal	O	63	0	7.67	7.57	7.14	3.89	5.67	6.20
$LiSiRu_2$	mp-865838	Cubic			0.001	5.07	4.28	4.28	4.28	4.28	4.28
$LuScRu_2$	mp-973433	Cubic			0	5.78	7.78	7.78	7.78	7.78	7.78
Lu_2NiRu	mp-865335	Cubic			0	5.44	7.02	7.22	7.22	7.15	7.15
$MgSnRu_2$	mp-1185980	Cubic			0	4.51	6.51	6.51	6.51	6.51	6.51
$MgVRu_2$	mp-1185620	Cubic			0.001	4.95	7.87	7.87	7.87	7.87	7.87
$MnBeRu_2$	mp-1185984	Cubic			1.989	5.03	6.90	6.90	6.90	6.90	6.90
$ScGaRu_2$	mp-867156	Cubic			0.004	5.32	6.65	6.65	6.65	6.65	6.65
$TaBeRu_2$	mp-867114	Cubic			0	6.48	8.03	8.03	8.03	8.03	8.03
$TiAlRu_2$	mp-866155	Cubic			0	6.12	7.91	7.91	7.91	7.91	7.91
Ti_2ReRu	mp-972275	Cubic			0	7.36	7.28	7.28	7.28	7.28	7.28
Ti_2TcRu	mp-865650	Cubic			0	6.32	7.63	7.63	7.63	7.63	7.63
$TmLuRu_2$	mp-983312	Cubic			0	5.80	7.29	7.30	7.30	7.30	7.30
USi_2Ru_2	mp-3388	Tetragonal	O	67 and 68	1.639	6.33	9.28	8.82	5.33	7.34	7.81
V_2OsRu	mp-971737	Cubic			0.249	6.26	5.66	5.66	5.66	5.66	5.66
V_2ReRu	mp-981365	Cubic			0.003	6.13	7.67	7.67	7.67	7.67	7.67
V_2TcRu	mp-865501	Cubic			0.007	5.87	7.26	7.26	7.26	7.26	7.26
$YbRu_3C$	mp-1206413	Cubic			0	6.48	8.04	8.04	8.04	8.04	8.04

[a] The synthesizability of the materials was determined by referencing the compositions provided in the ICSD. [b] The cohesive energies are obtained from the materials project database.

proxy for electromigration performance,[75,76] this strong correlation indicates that compounds with higher cohesive energy inherently possess enhanced interconnect reliability.

The trend of increasing $\rho_{avg} \times \lambda$ with larger effective atomic radii can be fundamentally rationalized through the relationship between real-space lattice dimensions and reciprocal-space electronic structure. While compound formation inherently modifies the periodic atomic potential and can alter the total valence electron concentration, the geometric volume effect plays a dominant role when comparing materials with similar Fermi surface topologies. Under the condition that the fundamental band structure is largely preserved, the incorporation of larger atoms inherently expands the real-space lattice parameters, which subsequently decreases the volumetric electron density. According to Luttinger's theorem,[77,78] the volume enclosed by the Fermi surface is strictly proportional to the particle density. Consequently, this real-space expansion inversely contracts the reciprocal-space Brillouin zone, which inherently bounds and effectively reduces the cross-sectional area of the Fermi surface.[79] Given that the effective Fermi surface area correlates with electrical conductivity,[80] this geometric contraction provides a compelling physical rationale for how increased cell volume degrades intrinsic transport performance. In addition to the average structural dimensions, we evaluated the variance descriptors to understand the impact of elemental size mismatch (Fig. 5b). The variance in the vdw_radius_uff shows a positive correlation (r = 0.40) with $\rho_{avg} \times \lambda$. This analytically demonstrates that compounds formed between elements with a large atomic size discrepancy tend to exhibit higher resistivity factors. Indeed, referring back to the distribution of binary compounds in Fig. 3, constituents with atomic radii similar to that of Ru—predominantly those located nearby in the periodic table such as Ir, Rh, Os and Tc—exhibited superior transport characteristics, corroborating this descriptor trend.

These theoretical rationales are directly supported by our electronic structure analysis. Notably, compounds sharing the same crystal structure and similar Fermi surface topology exhibit closely grouped $\rho_{avg} \times \lambda$ values. For instance, as

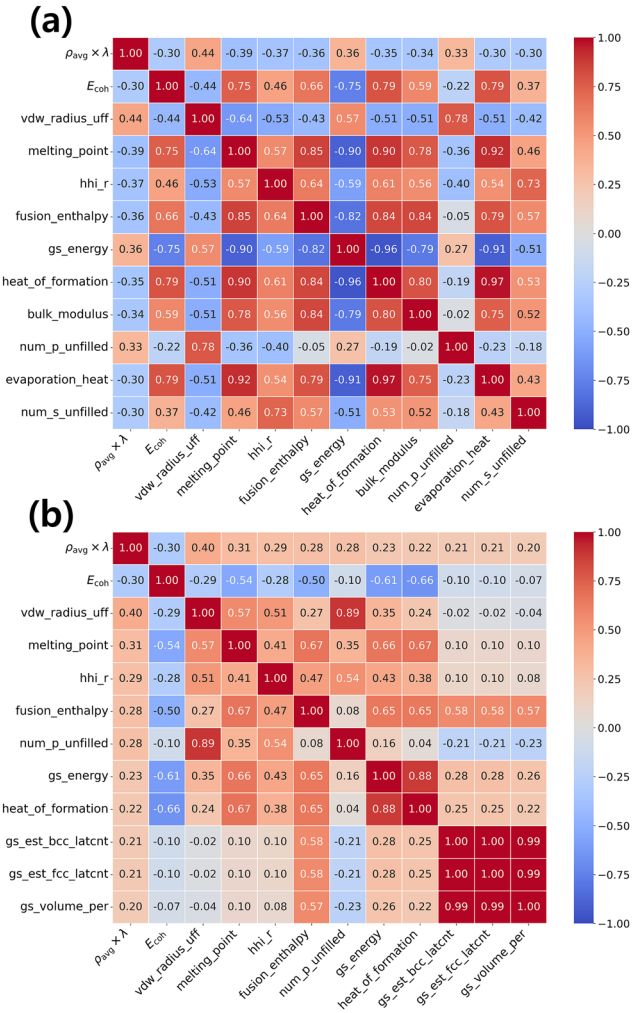

Fig. 5 Pearson correlation heatmap of compositional descriptors for binary compounds. (a) The matrix illustrates the correlation coefficients between the top 10 average-related compositional features extracted *via* the XenonPy toolkit and the primary screening metrics: $\rho_0 \times \lambda$ and E_{coh}. (b) The matrix illustrates the correlation coefficients between the top 10 variance-related compositional features and the same screening metrics.

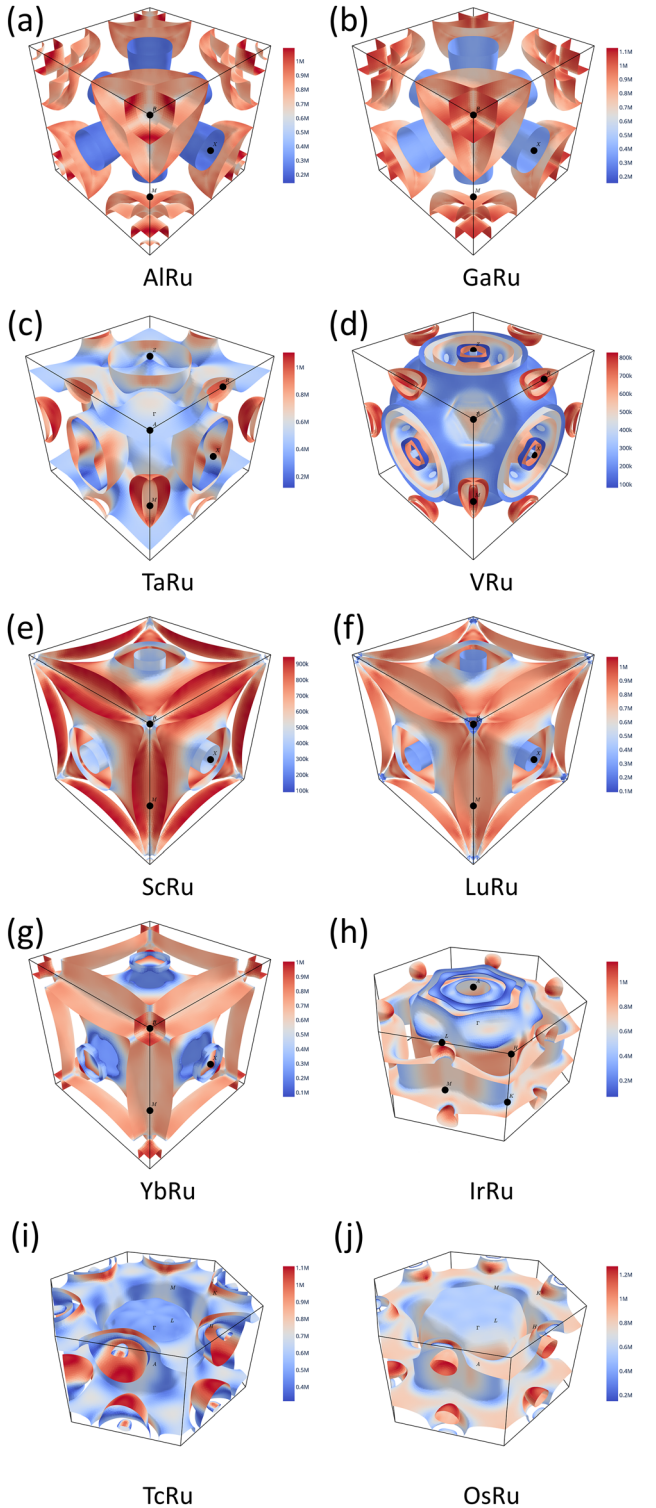

Fig. 6 Fermi surface topologies of selected binary Ru compounds. The calculated Fermi surface is categorized by their underlying crystal symmetry: (a)–(g) face-centered cubic (FCC) derived structures and (h)–(j) hexagonal close-packed (HCP) derived structures. The color mapping indicates the Fermi velocity distribution on the surface.

illustrated in Fig. 6, among 1 : 1 binary compounds, AlRu, GaRu, and TaRu share a face-centered cubic (FCC)-derived structure with analogous Fermi surface morphologies and accordingly cluster within a comparable $\rho_{avg} \times \lambda$ range. Similarly, ScRu, LuRu, and YbRu also adopt an FCC-derived structure with mutually similar, yet distinctly different, Fermi surface morphologies from the former group, resulting in their own closely grouped $\rho_{avg} \times \lambda$ values. However, even within this isostructural group, compounds incorporating larger atoms (*e.g.*, Lu and Yb) exhibit higher values, which perfectly aligns with our average cell expansion analysis. Conversely, VRu, which adopts the same FCC structure but exhibits a distinctly different Fermi surface morphology, displays a somewhat different transport value. An analogous topological clustering is observed among hexagonal close-packed (HCP) structured compounds: IrRu, OsRu, and TcRu share highly similar Fermi surface features and correspondingly cluster within a very narrow, highly conductive range. Consequently, from a practical materials design perspective, selecting constituent elements

with similar atomic radii to minimize lattice mismatch, while simultaneously keeping the overall cell volume small to prevent Brillouin zone contraction, represents a highly effective strategy for minimizing intrinsic transport degradation during compound formation or alloying.

While elemental metals often define upper bounds in intrinsic performance metrics, compound formation can offer distinct integration-driven advantages that are not captured by these indicators alone. In the context of interconnect technology, prior studies have demonstrated that specific compound phases can exhibit superior adhesion to dielectrics, suppress atomic diffusion, and enable self-forming barrier or liner behaviors.[81–86] These attributes are critical for enhancing reliability and allowing for reduced barrier/liner thickness—a key requirement at extremely scaled dimensions where interfacial effects dominate the effective resistance. Moreover, exploring compound compositions substantially expands the accessible materials space beyond the limited set of elemental conductors, enabling the identification of candidates that strike a more favorable balance between intrinsic electrical performance and integration-relevant feasibility. In this context, the present results provide a meaningful framework for guiding future interconnect material exploration beyond elemental systems.

4 Conclusions

In this study, we conducted a comprehensive high-throughput screening of Ru-based binary, ternary, and quaternary compounds to identify promising candidates for next-generation interconnect applications. By evaluating 2106 initial phases based on first-principles calculations, we identified 61 viable candidates—23 binary and 38 ternary compounds—that satisfy rigorous stability and performance criteria relative to the industry-standard Cu. Our analysis highlights several experimentally synthesized candidates, including the binary compound AlRu, which has already been investigated as a potential interconnect material. Regarding quaternary systems, although no candidates were identified within our specific screening window, this outcome is significantly influenced by the rigorous structural constraints applied during our screening process, where a substantial number of candidates were preemptively excluded due to the increased stoichiometric complexity inherent in moving from binary to quaternary systems. From a performance standpoint, our results indicate that while elemental Ru sets a high benchmark in intrinsic electronic transport, compound formation offers a pathway to engineer materials with distinct advantages. With the exception of Ir_3Ru, most screened compounds do not surpass the performance distribution of elemental Ru; however, the value of compound formation extends beyond simple resistivity minimization. The screened compounds offer potential integration-driven advantages, such as enhanced adhesion, chemical stability, and the possibility of barrierless integration, which are essential for minimizing the effective resistance in sub-nanometer interconnect stacks. Furthermore, our descriptor and Fermi surface topology analyses reveal that the overall cell volume is one of the primary structural factors governing intrinsic transport degradation upon compound formation. Additionally, as observed in compounds formed with elements adjacent to Ru in the periodic table—such as Ir, Os, Rh, and Tc—minimizing the atomic size mismatch between constituent elements can further mitigate transport degradation, providing an effective design principle for screening next-generation interconnect compounds. Consequently, this study provides a foundational roadmap for expanding the materials design space, guiding the industry transition from elemental conductors to optimized compound systems that balance intrinsic performance with process feasibility. Future investigations will focus on providing a more comprehensive understanding of transport properties under realistic device geometries and confinement conditions. Integrating additional scattering mechanisms, such as grain boundary and surface scattering, will be crucial, particularly given their pronounced impact on thin film resistivity. Leveraging advanced computational frameworks like EPW[87] or PERTURBO[88] to quantify these complex scattering phenomena, including electron–phonon interactions, will significantly advance the performance classification and practical application of these materials as next-generation interconnects.

Author contributions

Gyungho Maeng: data curation, formal analysis, investigation, methodology, software, validation, visualization, and writing – original draft. Subeen Lim: formal analysis and methodology. Bonggeun Shong: funding acquisition, validation, and writing – review & editing. Yeonghun Lee: supervision, conceptualization, project administration, formal analysis, funding acquisition, methodology, validation, and writing – review & editing.

Conflicts of interest

The authors declare that they have no known competing financial interest or personal relationships that could have appeared to influence the work reported in this paper.

Data availability

All data supporting the findings of this study have been obtained by the authors and presented within the main text and supplementary information (SI). Details of simulation tools and packages (*e.g.*, VASP, Materials Project) and computational methodologies, including relevant equations, are provided in the main text. While the conductivity-based averaging scheme is detailed in the main text, the SI provides complementary data using the alternative resistivity-based averaging scheme (Fig. S1–S3), as well as an expanded performance benchmarking against constituent elemental metals (Fig. S4) and the extracted compositional descriptors used for the correlation

analysis (Table S1). See DOI: https://doi.org/10.1039/d6tc00235h.

Acknowledgements

This work was supported by the Technology Innovation Program [Public-private joint investment semiconductor R&D program (K-CHIPS) to foster high-quality human resources] [no. RS-2023-00236667, high performance Ru–TiN interconnects *via* high temperature atomic layer deposition (ALD) and development on new interconnect materials based on ALD] funded by the Ministry of Trade, Industry & Energy (MOTIE, Korea) (no. 1415187401). This work was supported by the National Supercomputing Center with supercomputing resources including technical support (no. KSC-2025-CRE-0054).

References

1 K. Fuchs, *Math. Proc. Cambridge Philos. Soc.*, 1938, **34**, 100–108.
2 E. H. Sondheimer, *Adv. Phys.*, 2001, **50**, 499–537.
3 A. F. Mayadas and M. Shatzkes, *Phys. Rev. B: Condens. Matter Mater. Phys.*, 1970, **1**, 1382–1389.
4 T. Markussen, S. Aboud, A. Blom, N. A. Lanzillo, T. Gunst, J. Cobb, T. M. Philip and R. R. Robison, *2020 IEEE International Interconnect Technology Conference (IITC)*, IEEE, San Jose, CA, USA, 2020, pp. 76–78.
5 D. Gall, *J. Appl. Phys.*, 2020, **127**, 050901.
6 H.-D. Liu, Y.-P. Zhao, G. Ramanath, S. P. Murarka and G.-C. Wang, *Thin Solid Films*, 2001, **384**, 151–156.
7 S. Dutta, K. Sankaran, K. Moors, G. Pourtois, S. Van Elshocht, J. Bömmels, W. Vandervorst, Z. Tőkei and C. Adelmann, *J. Appl. Phys.*, 2017, **122**, 025107.
8 S. Dutta, K. Moors, M. Vandemaele and C. Adelmann, *IEEE Electron Device Lett.*, 2018, **39**, 268–271.
9 J. H. Moon, S. Kim, T. Kim, Y. S. Jeon, Y. Kim, J.-P. Ahn and Y. K. Kim, *J. Mater. Sci. Technol.*, 2022, **105**, 17–25.
10 D. Gall, *J. Appl. Phys.*, 2016, **119**, 085101.
11 P. Kapur, J. P. McVittie and K. C. Saraswat, *IEEE Trans. Electron Devices*, 2002, **49**, 590–597.
12 R. Saligram, S. Datta and A. Raychowdhury, *IEEE Trans. Circuits Syst.*, 2022, **69**, 4610–4618.
13 M. H. van der Veen, N. Heyler, O. V. Pedreira, I. Ciofi, S. Decoster, V. V. Gonzalez, N. Jourdan, H. Struyf, K. Croes, C. J. Wilson and Zs Tőkei, *2018 IEEE International Interconnect Technology Conference (IITC)*, 2018, pp. 172–174.
14 L. Gong Wen, C. Adelmann, O. V. Pedreira, S. Dutta, M. Popovici, B. Briggs, N. Heylen, K. Vanstreels, C. J. Wilson, S. Van Elshocht, K. Croes, J. Bommels and Z. Tokei, *2016 IEEE International Interconnect Technology Conference/Advanced Metallization Conference (IITC/AMC)*, IEEE, San Jose, CA, USA, 2016, pp. 34–36.
15 Y. Kotsugi, S.-M. Han, Y.-H. Kim, T. Cheon, D. K. Nandi, R. Ramesh, N.-K. Yu, K. Son, T. Tsugawa, S. Ohtake, R. Harada, Y.-B. Park, B. Shong and S.-H. Kim, *Chem. Mater.*, 2021, **33**, 5639–5651.
16 C.-C. Yang, T. Spooner, S. Ponoth, K. Chanda, A. Simon, C. Lavoie, M. Lane, C.-K. Hu, E. Liniger, L. Gignac, T. Shaw, S. Cohen, F. McFeely and D. Edelstein, *2006 International Interconnect Technology Conference*, IEEE, Burlingame, CA, 2006, pp. 187–190.
17 H. Y. Huang, C. H. Hsieh, S. M. Jeng, H. J. Tao, M. Cao and Y. J. Mii, *2010 IEEE International Interconnect Technology Conference*, IEEE, Burlingame, CA, USA, 2010, pp. 1–3.
18 J. Rullan, T. Ishizaka, F. Cerio, S. Mizuno, Y. Mizusawa, T. Ponnuswamy, J. Reid, A. McKerrow and C.-C. Yang, *2010 IEEE International Interconnect Technology Conference*, IEEE, Burlingame, CA, USA, 2010, pp. 1–3.
19 C.-C. Yang, S. Cohen, T. Shaw, P.-C. Wang, T. Nogami and D. Edelstein, *IEEE Electron Device Lett.*, 2010, **31**, 722–724.
20 D. Wan, S. Paolillo, N. Rassoul, B. K. Kotowska, V. Blanco, C. Adelmann, F. Lazzarino, M. Ercken, G. Murdoch, J. Bömmels, C. J. Wilson and Z. Tökei, *2018 IEEE International Interconnect Technology Conference (IITC)*, 2018, pp. 10–12.
21 C. Penny, K. Motoyama, S. Ghosh, T. Bae, N. Lanzillo, S. Sieg, C. Park, L. Zou, H. Lee, D. Metzler, J. Lee, S. Cho, M. Shoudy, S. Nguyen, A. Simon, K. Park, L. Clevenger, B. Anderson, C. Child, T. Yamashita, J. Arnold, T. Wu, T. Spooner, K. Choi, K.-I. Seo and D. Guo, *2022 International Electron Devices Meeting (IEDM)*, IEEE, San Francisco, CA, USA, 2022, pp. 12.1.1–12.1.4.
22 A. Dutta, A. Peer, C. Jezewski, S. Siddiqui, I. Jenkins, E. Khora, G. Auluck, Y. Huang, F. Bedoya, N. Kabir, S. Mocherla, P. R. Saha, L. Shoer, K. Chan, A. Tanneeru, J. Gupta, V. B. Jeevendrakumar, D. Collins, S. Madhusoodhanan, J. Bielefeld, W. Brezinski, R. Fayad, S. Sukrittanon, S. Naskar, S. Kosaraju, N. Nair, G. Singh, J. D. Silva, C. Engel, N. Franco, B. Krist, J. Wang, M. Metz and M. Kobrinsky, *2024 IEEE International Electron Devices Meeting (IEDM)*, 2024, pp. 1–4.
23 E. Cho, W.-J. Son, S. Lee, H.-S. Do, K. Min and D. S. Kim, *J. Mater. Chem. C*, 2025, **13**, 7772–7784.
24 P. Zheng and D. Gall, *J. Appl. Phys.*, 2017, **122**, 135301.
25 K. Sankaran, S. Clima, M. Mees and G. Pourtois, *ECS J. Solid State Sci. Technol.*, 2015, **4**, N3127–N3133.
26 S. Kumar, C. Multunas, B. Defay, D. Gall and R. Sundararaman, *Phys. Rev. Mater.*, 2022, **6**, 085002.
27 M. Zhang and C. Adelmann, *J. Appl. Phys.*, 2025, **138**, 090902.
28 G. Kresse and J. Hafner, *Phys. Rev. B: Condens. Matter Mater. Phys.*, 1993, **47**, 558–561.
29 G. Kresse and J. Furthmüller, *Phys. Rev. B: Condens. Matter Mater. Phys.*, 1996, **54**, 11169–11186.
30 J. P. Perdew, K. Burke and M. Ernzerhof, *Phys. Rev. Lett.*, 1996, **77**, 3865–3868.
31 K. Lejaeghere, G. Bihlmayer, T. Björkman, P. Blaha, S. Blügel, V. Blum, D. Caliste, I. E. Castelli, S. J. Clark, A. Dal Corso, S. De Gironcoli, T. Deutsch, J. K. Dewhurst, I. Di Marco, C. Draxl, M. Dułak, O. Eriksson, J. A. Flores-

Livas, K. F. Garrity, L. Genovese, P. Giannozzi, M. Giantomassi, S. Goedecker, X. Gonze, O. Grånäs, E. K. U. Gross, A. Gulans, F. Gygi, D. R. Hamann, P. J. Hasnip, N. A. W. Holzwarth, D. Iuşan, D. B. Jochym, F. Jollet, D. Jones, G. Kresse, K. Koepernik, E. Küçükbenli, Y. O. Kvashnin, I. L. M. Locht, S. Lubeck, M. Marsman, N. Marzari, U. Nitzsche, L. Nordström, T. Ozaki, L. Paulatto, C. J. Pickard, W. Poelmans, M. I. J. Probert, K. Refson, M. Richter, G.-M. Rignanese, S. Saha, M. Scheffler, M. Schlipf, K. Schwarz, S. Sharma, F. Tavazza, P. Thunström, A. Tkatchenko, M. Torrent, D. Vanderbilt, M. J. Van Setten, V. Van Speybroeck, J. M. Wills, J. R. Yates, G.-X. Zhang and S. Cottenier, *Science*, 2016, **351**, aad3000.

32 P. E. Blöchl, *Phys. Rev. B: Condens. Matter Mater. Phys.*, 1994, **50**, 17953–17979.

33 A. Dal Corso, *Phys. Rev. B: Condens. Matter Mater. Phys.*, 2012, **86**, 085135.

34 A. Jain, S. P. Ong, G. Hautier, W. Chen, W. D. Richards, S. Dacek, S. Cholia, D. Gunter, D. Skinner, G. Ceder and K. A. Persson, *APL Mater.*, 2013, **1**, 011002.

35 M. K. Horton, P. Huck, R. X. Yang, J. M. Munro, S. Dwaraknath, A. M. Ganose, R. S. Kingsbury, M. Wen, J. X. Shen, T. S. Mathis, A. D. Kaplan, K. Berket, J. Riebesell, J. George, A. S. Rosen, E. W. C. Spotte-Smith, M. J. McDermott, O. A. Cohen, A. Dunn, M. C. Kuner, G.-M. Rignanese, G. Petretto, D. Waroquiers, S. M. Griffin, J. B. Neaton, D. C. Chrzan, M. Asta, G. Hautier, S. Cholia, G. Ceder, S. P. Ong, A. Jain and K. A. Persson, *Nat. Mater.*, 2025, **24**, 1522–1532.

36 W. Sun, S. T. Dacek, S. P. Ong, G. Hautier, A. Jain, W. D. Richards, A. C. Gamst, K. A. Persson and G. Ceder, *Sci. Adv.*, 2016, **2**, e1600225.

37 A. Lee, S. Sarker, J. E. Saal, L. Ward, C. Borg, A. Mehta and C. Wolverton, *Commun. Mater.*, 2022, **3**, 73.

38 S. P. Ong, W. D. Richards, A. Jain, G. Hautier, M. Kocher, S. Cholia, D. Gunter, V. L. Chevrier, K. A. Persson and G. Ceder, *Comput. Mater. Sci.*, 2013, **68**, 314–319.

39 G. K. H. Madsen and D. J. Singh, *Comput. Phys. Commun.*, 2006, **175**, 67–71.

40 G. K. H. Madsen, J. Carrete and M. J. Verstraete, *Comput. Phys. Commun.*, 2018, **231**, 140–145.

41 S. Lim, Y. Kim, G. Maeng and Y. Lee, *J. Phys.: Condens. Matter*, 2026, **38**, 015503.

42 S. Nagata and M. Nakajima, *Phys. B*, 1993, **192**, 228–232.

43 Z. Hashin and S. Shtrikman, *Phys. Rev.*, 1963, **130**, 129–133.

44 K. Moors, K. Sankaran, G. Pourtois and C. Adelmann, *Phys. Rev. Mater.*, 2022, **6**, 123804.

45 S. Park, S. Kang, G. Kim, J. Moon, K. Lee and J. Chang, *IEEE Trans. Electron Devices*, 2025, **72**, 5703–5709.

46 L.-E. Edshammar, H. Iwamoto, G. Bergson, L. Ehrenberg, J. Brunvoll, E. Bunnenberg, C. Djerassi and R. Records, *Acta Chem. Scand.*, 1966, **20**, 427–431.

47 T. D. Boniface and L. A. Cornish, *J. Alloys Compd.*, 1996, **234**, 275–279.

48 W. Jeitschko, H. Holleck, H. Nowotny and F. Benesovsky, *Monatsh. Chem.*, 1963, **94**, 838–840.

49 R. P. Elliott, *Laves phases of the rare earths with transition elements*, Illinois Inst. of Tech., IIT Research Inst., Chicago, IL (United States), 1964.

50 V. N. Eremenko, V. G. Khorujaya, P. S. Martsenyuk and K. Ye Korniyenko, *J. Alloys Compd.*, 1995, **217**, 213–217.

51 V. G. Khoruzhaya and K. E. Kornienko, *Powder Metall. Met. Ceram.*, 2001, **40**, 362–373.

52 E. Raub, H. Beeskow and W. Fritzsche, *Int. J. Mater. Res.*, 1963, **54**, 451–454.

53 B. H. Chen and H. F. Franzen, *J. Less-Common Met.*, 1990, **157**, 37–45.

54 H. Holleck and H. Kleykamp, *J. Nucl. Mater.*, 1970, **35**, 158–166.

55 H. R. Ott, F. Hulliger, H. Rudigier and Z. Fisk, *Phys. Rev. B: Condens. Matter Mater. Phys.*, 1985, **31**, 1329–1333.

56 E. Raub and W. Fritzsche, *Int. J. Mater. Res.*, 1963, **54**, 21–23.

57 R. M. Waterstrat and R. C. Manuszewski, *J. Less-Common Met.*, 1976, **48**, 151–158.

58 A. Landelli and A. Palenzona, *Rev. Chim. Miner.*, 1976, **13**, 55–61.

59 Y.-Y. Fang, Y.-H. Tsai, Y.-L. Chen, D.-J. Jhan, M.-Y. Lu, P. Y. Keng and S.-Y. Chang, *Appl. Phys. Lett.*, 2024, **124**, 142108.

60 A. A. Menovsky, *J. Magn. Magn. Mater.*, 1988, **76–77**, 631–636.

61 M. J. Besnus, A. Essaihi, N. Hamdaoui, G. Fischer, J. P. Kappler, A. Meyer, J. Pierre, P. Haen and P. Lejay, *Phys. B*, 1991, **171**, 350–352.

62 W. Jeitschko, R. Glaum and L. Boonk, *J. Solid State Chem.*, 1987, **69**, 93–100.

63 K. Hiebl, C. Horvath, P. Rogl and M. J. Sienko, *J. Magn. Magn. Mater.*, 1983, **37**, 287–296.

64 C. Godart, C. Ammarguellat, N. Wetta, G. Krill and J. C. Achard, *J. Magn. Magn. Mater.*, 1987, **63–64**, 527–528.

65 M. Francois, G. Venturini, J. F. Marêché, B. Malaman and B. Roques, *J. Less-Common Met.*, 1985, **113**, 231–237.

66 I. Felner and I. Nowik, *J. Phys. Chem. Solids*, 1985, **46**, 681–687.

67 A. A. Menovsky, A. C. Moleman, G. E. Snel, T. J. Gortenmulder, H. J. Tan and T. T. M. Palstra, *J. Cryst. Growth*, 1986, **79**, 316–321.

68 T. E. Mason, B. D. Gaulin, J. D. Garrett, Z. Tun, W. J. L. Buyers and E. D. Isaacs, *Phys. Rev. Lett.*, 1990, **65**, 3189–3192.

69 B. C. Odegard and C. H. Cadden, *17th IEEE/NPSS Symposium Fusion Engineering (Cat. No. 97CH36131)*, 1997, vol. 2, pp. 896–900.

70 N. Sakamoto and K. Hiroshi, *J. Nucl. Mater.*, 1997, **233–237**, 609–611.

71 L. L. Snead and S. J. Zinkle, *AIP Conf. Proc.*, 2005, **746**, 768–775.

72 O. D. Neĭkov, S. S. Naboychenko and I. B. Murashova, *Handbook of Non-Ferrous Metal Powders*, Elsevier Ltd, 2nd edn, 2019.

73 G. Maeng and Y. Lee, *Electron. Mater. Lett.*, 2026, DOI: 10.1007/s13391-026-00632-9.

74 H. Yamada, C. Liu, S. Wu, Y. Koyama, S. Ju, J. Shiomi, J. Morikawa and R. Yoshida, *ACS Cent. Sci.*, 2019, **5**, 1717–1730.

75 C. Adelmann, L. G. Wen, A. P. Peter, Y. K. Siew, K. Croes, J. Swerts, M. Popovici, K. Sankaran, G. Pourtois, S. Van Elshocht, J. Bömmels and Z. Tőkei, *IEEE International Interconnect Technology Conference*, 2014, pp. 173–176.
76 K. Croes, Ch Adelmann, C. J. Wilson, H. Zahedmanesh, O. V. Pedreira, C. Wu, A. Lesniewska, H. Oprins, S. Beyne, I. Ciofi, D. Kocaay, M. Stucchi and Zs Tokei, *2018 IEEE International Electron Devices Meeting (IEDM)*, IEEE, San Francisco, CA, 2018, p. 5.3.1–5.3.4.
77 J. M. Luttinger and J. C. Ward, *Phys. Rev.*, 1960, **118**, 1417–1427.
78 J. M. Luttinger, *Phys. Rev.*, 1960, **119**, 1153–1163.
79 S. Kang, S. Park and J. Chang, *J. Mater. Chem. C*, 2026, DOI: 10.1039/D5TC04036A.
80 Y. Hu, P. Conlin, Y. Lee, D. Kim and K. Cho, *J. Mater. Chem. C*, 2022, **10**, 5627–5635.
81 J. Koike, M. Haneda, J. Iijima and M. Wada, *2006 International Interconnect Technology Conference*, IEEE, Burlingame, CA, 2006, pp. 161–163.
82 J. Koike, T. Kuge, L. Chen and M. Yahagi, *2021 IEEE International Interconnect Technology Conference (IITC)*, IEEE, Kyoto, Japan, 2021, pp. 1–3.
83 C. Kim, G. Kang, Y. Jung, J.-Y. Kim, G.-B. Lee, D. Hong, Y. Lee, S.-G. Hwang, I.-H. Jung and Y.-C. Joo, *Sci. Rep.*, 2022, **12**, 12291.
84 T. Kuge, M. Yahagi and J. Koike, *J. Alloys Compd.*, 2022, **918**, 165615.
85 M. Zhang and D. Gall, *IEEE Trans. Electron Devices*, 2024, **71**, 3252–3257.
86 M. Iwabuchi, Y. Suto and J. Koike, *Appl. Surf. Sci.*, 2026, **720**, 165148.
87 H. Lee, S. Poncé, K. Bushick, S. Hajinazar, J. Lafuente-Bartolome, J. Leveillee, C. Lian, J.-M. Lihm, F. Macheda, H. Mori, H. Paudyal, W. H. Sio, S. Tiwari, M. Zacharias, X. Zhang, N. Bonini, E. Kioupakis, E. R. Margine and F. Giustino, *npj Comput Mater*, 2023, **9**, 156.
88 J.-J. Zhou, J. Park, I.-T. Lu, I. Maliyov, X. Tong and M. Bernardi, *Comput. Phys. Commun.*, 2021, **264**, 107970.